nature communications

Article

https://doi.org/10.1038/s41467-025-63365-7

Electrosynthesis of NH_3 from low-concentration NO on cascade dual-site catalysts in neutral media

Received: 21 April 2025

Accepted: 19 August 2025

Published online: 26 September 2025

Check for updates

Xiaoxi Guo[1,2,3,8], Tongwei Wu[4,8], Hengfeng Li[3], Yanning Zhang[4], Chao Ma[5], Hongmei Li[1], Liyuan Chai[6], Haitao Zhao[7] & Min Liu[1,6]

Electrosynthesis of NH_3 from low-concentration NO (NORR) in neutral media offers a sustainable nitrogen fixation strategy but is hindered by weak NO adsorption, slow water dissociation, and sluggish hydrogenation kinetics. Herein, we propose an intriguing strategy that successfully overcomes these limitations through using an electron-donating motif to modulate NO-affinitive catalysts, thereby creating dual active site with synergistic functionality. Specifically, we integrate electron-donating nanoparticles into a Fe single-atom catalyst (Fe_{SAC}), where Fe sites ensure strong NO adsorption, while electron-donating motifs promote water dissociation and NO hydrogenation. In situ X-ray absorption spectroscopy (XAS), in situ attenuated total reflection-infrared spectroscopy (ATR-IR), and theoretical calculations reveal that electron-donating motifs increase Fe site electron density, strengthening NO adsorption. Additionally, these motifs also promote water dissociation, supplying protons to lower the NO hydrogenation barrier. This synergistic interplay enables a cascade reaction mechanism, delivering a remarkable Faradaic efficiency (FE) of 90.3% and a NH_3 yield rate of 709.7 μg h^{-1} $mg_{cat.}^{-1}$ under 1.0 vol% NO in neutral media, outperforming pure Fe_{SAC} (NH_3 yield rate: 444.2 μg h^{-1} $mg_{cat.}^{-1}$, FE: 56.6%) and prior to systems operating under high NO concentrations. Notably, the high NH_3 yield of 3207.7 μg h^{-1} $mg_{cat.}^{-1}$ is achieved in a membrane electrode assembly (MEA) electrolyzer under a 1.0 vol% NO. This work establishes an inspirational paradigm in NORR by simultaneously enhancing NO adsorption, water dissociation, and hydrogenation kinetics, providing a scalable route for efficient NH_3 electrosynthesis from dilute NO sources.

Nitric oxide (NO) is a harmful atmospheric pollutant primarily emitted from industrial processes and vehicle exhaust, posing severe environmental and health risks[1–6]. Selective catalytic reduction (SCR) is the predominant method for mitigating NO emissions[6–10]. Nevertheless, it requires temperatures of 300-400 °C and uses ammonia as a reducing agent, thus restricting its efficiency under near-ambient conditions and failing to generate any value-added products. Electrochemical NO reduction (NORR) under mild conditions, utilizing renewable electricity and water, offers a sustainable route to both NO removal and ammonia (NH_3) production—an essential fertilizer and potential hydrogen carrier—via a carbon-free process[11–13]. Large-scale NORR requires neutral water conditions to enable earth-abundant transition metal catalysts, which are unstable in acidic media, and to facilitate direct seawater use without desalination[14–18]. However, its efficiency in neutral media is severely restricted by low NO solubility, sluggish water dissociation, and slow NO hydrogenation kinetics.

A full list of affiliations appears at the end of the paper. e-mail: minliu@csu.edu.cn

Most current research focuses on engineering electron-deficient sites to strengthen NO adsorption for NORR under neutral media, even at low NO concentrations[19–26]. Among these catalysts, Fe-based catalysts exhibit remarkable efficiency in enhancing the performance of low-concentration NORR[22,25,26]. This becomes particularly effective when Fe sites are in a low oxidation state with sharp d-state defect features, enabling energy-aligned orbital configurations that facilitate the adsorption and activation of NO molecules[23]. Moreover, as one of the most cost-effective and abundant elements in the earth[27], Fe also plays a pivotal role in biological nitrogenases, enabling efficient natural nitrogen fixation[28]. However, the current approach of enhancing NO affinity on catalysts overlooks the critical challenge of inherently slow water dissociation and NO hydrogenation kinetics in neutral media.

Electron-donating materials have demonstrated significant catalytic efficiency in water dissociation reactions[29,30], which are essential for supplying protons to promote NO hydrogenation[21–24]. Inspired by aforementioned guidance, we propose an innovative and universal strategy to improve neutral NORR performance by integrating electron-donating motifs into NO-affinitive catalysts, forming a dual-active-site architecture with synergistic functionality. To demonstrate this strategy and its underlying mechanism, we selected Pt nanoparticles as the electron donor, incorporated into an Fe single-atom catalyst (Fe_{SAC}) with NO-affinitive ability, as a representative case for detailed analysis. In situ X-ray absorption spectroscopy (XAS), attenuated total reflection-infrared spectroscopy (ATR-IR), and density functional theory (DFT) calculations confirmed that Pt_{NPs} serve as electron donors, increasing the electron density at the Fe sites for stronger NO adsorption, while also facilitating water dissociation to supply protons and significantly promoting the subsequent hydrogenation of NO intermediate. The synergistic interplay between these dual sites enables a cascade reaction mechanism. As a result, the Pt_{NPs}/Fe_{SAC} catalyst achieved a NH_3 yield rate of 709.7 μg h^{-1} $mg_{cat.}^{-1}$ and a Faraday efficiency (FE) of 90.3% at −0.6 V under 1.0 vol% NO/Ar in neutral media, outperforming Fe_{SAC} alone (NH_3 yield rate: 444.2 μg h^{-1} $mg_{cat.}^{-1}$, FE: 56.6%) and surpassing previously reported NORR systems under high NO concentrations (above 10%) in various medias. Notably, in a membrane electrode assembly (MEA) electrolyzer, the system achieved the NH_3 yield of 3207.7 μg h^{-1} $mg_{cat.}^{-1}$. This approach was successfully extended to other electron-donating nanoparticles, such as Au, highlighting its broad applicability for efficient NORR in neutral media.

Results and discussion

Theoretical calculations

DFT calculations were performed to understand the mechanism underlying the enhanced NORR activity. Fe single atoms coordinated with pyridine-4N in graphene (FeN_4) were chosen as the catalyst model due to their high stability (Fig. 1a)[31]. To simulate the nanoparticle environment, nine Pt atoms were introduced into the FeN_4 structure (FeN_4-Pt, Fig. 1b). Before Pt loading, Fe single atom in FeN_4 exhibited partially unoccupied orbitals above the Fermi level (Fig. 1c). After Pt loading, these unoccupied orbitals shifted towards the Fermi level, indicating electron injection into Fe (Fig. 1d). Bader charge analysis confirmed that Fe received ~0.16e⁻ (Fig. 1e), increasing its electron density and reactivity[32]. In Supplementary Fig. 2, the charge density difference analysis of Fe site in FeN_4-Pt demonstrated markedly increased electron density accumulation relative to those in FeN_4, suggesting that Pt species exhibit electron-donating characteristics that enhance the electronic environment at Fe active centers.

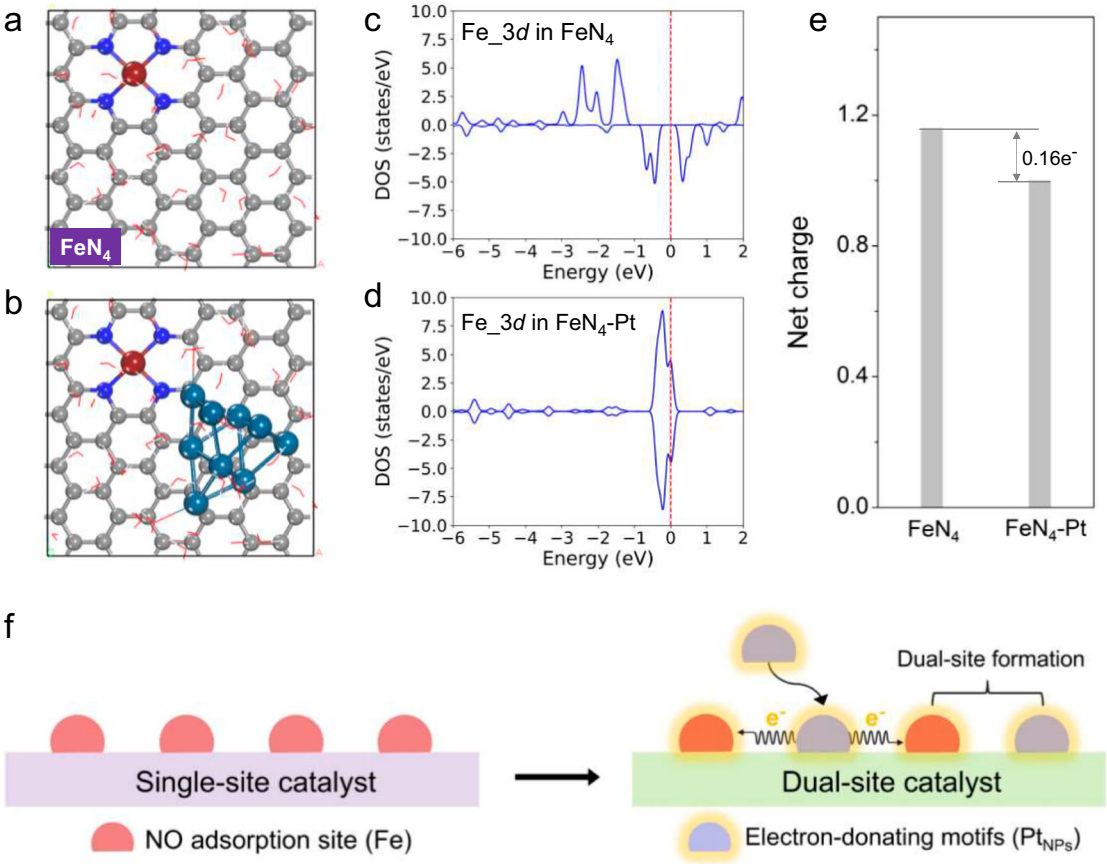

Fig. 1 | Theoretical calculations. Atom configurations of (**a**) FeN_4 and (**b**) FeN_4-Pt. Atom color-coding: brown, iron; blue, nitrogen; grey, carbon; cyan, platinum. Corresponding DOS plots of Fe atom in (**c**) FeN_4 and (**d**) FeN_4-Pt. **e** Bader charge analysis of Fe atom in FeN_4 and FeN_4-Pt, respectively. **f** Schematic diagram of dual site catalyst. Source data are provided as a Source Data file.

https://doi.org/10.1038/s41467-025-63365-7

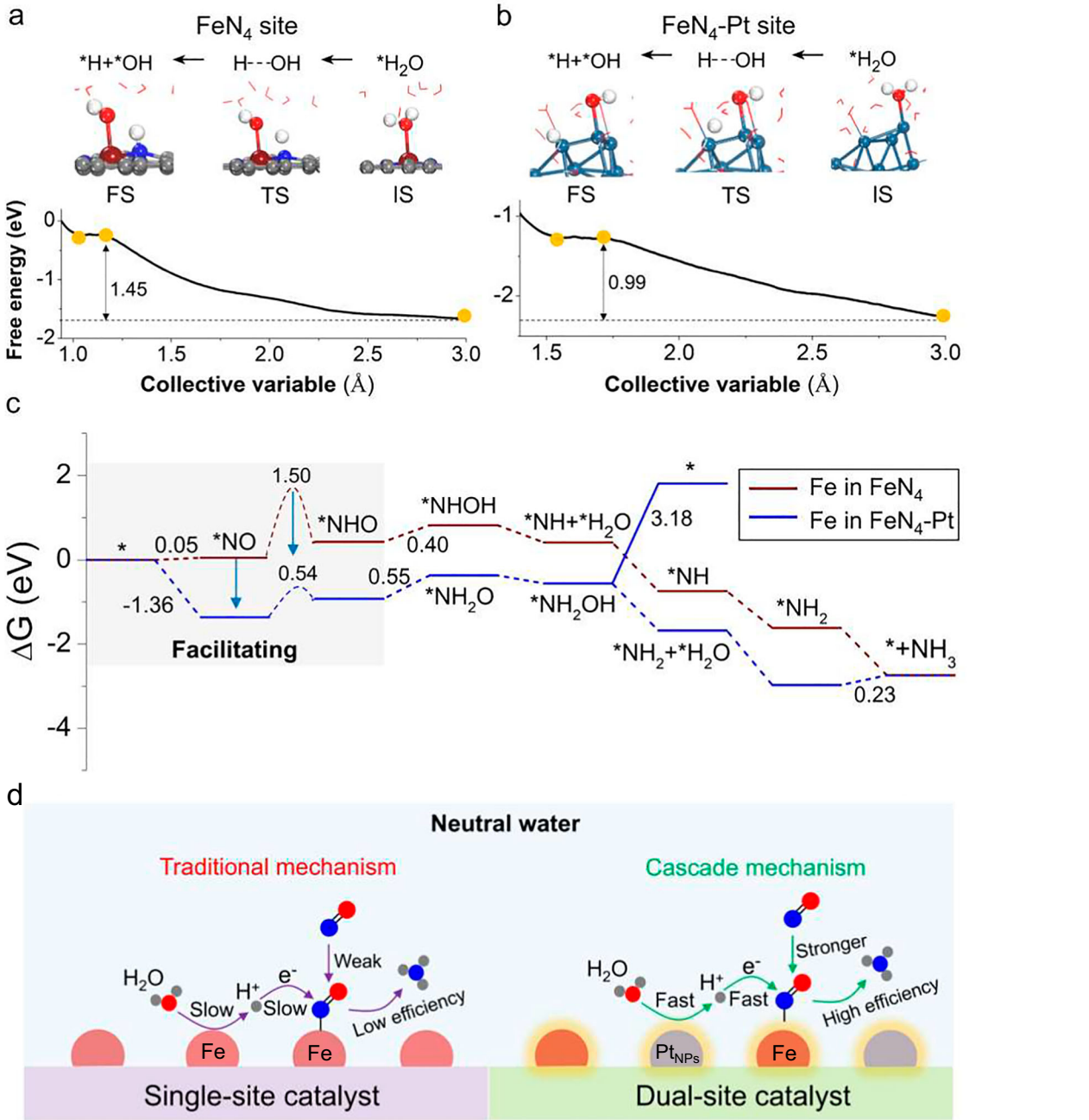

Fig. 2 | Reaction mechanism. The free energy of water dissociation on (**a**) FeN_4 and (**b**) FeN_4-Pt. Atom color-coding: brown, iron; blue, nitrogen; grey, carbon; cyan, platinum; white, hydrogen; red, oxygen. **c** The reaction free energies of NORR pathways on FeN_4 and FeN_4-Pt. **d** Comparation between traditional and cascade mechanisms. Source data are provided as a Source Data file.

Therefore, the incorporation of Pt nanoparticle into FeN_4 creates a dual active site (Fig.1f).

We firstly investigated water dissociation on both FeN_4 and FeN_4-Pt sites (Figs. 2a, b). On FeN_4 site, the dissociation of H_2O into *H and *OH required a free energy of 1.45 eV. However, in FeN_4-Pt, H_2O adsorbed at Pt sites, reducing the dissociation energy to 0.99 eV, demonstrating the role of Pt in facilitating proton supply for NORR.

Next, the free energy pathway for NO to NH_3 conversion was calculated and a significant enhancement in the NO adsorption capability on FeN_4-Pt (−1.36 eV) compared to FeN_4 (0.05 eV) was revealed (Fig. 2c). The first proton step (*NO → *HNO) was energetically favorable on both catalysts, but the activation barrier was reduced from 1.50 eV (FeN_4) to 0.54 eV (FeN_4-Pt). The second protonation led to the formation of $*NH_2O$ (FeN_4-Pt, $\Delta G = 0.55$ eV) instead of *HNOH (FeN_4, $\Delta G = 0.40$ eV), thus shifting the reaction pathway. The third protonation on FeN_4-Pt led to $*NH_2OH$ formation, but its high desorption energy (3.18 eV) made $*NH_2OH$ an unlikely byproduct. Instead, $*NH_2OH$ underwent hydrogenation to $*NH_2 + H_2O$, followed by an exothermic step to NH_3 ($\Delta G = 0.23$ eV).

Overall, Pt_{NPs} enhance NORR by donating electrons to Fe, strengthening NO adsorption, and accelerating water dissociation to supply protons for NO hydrogenation. This synergistic cascade mechanism significantly boosts NH_3 synthesis efficiency in neutral low-concentration NO conditions (Fig. 2d).

Catalyst characterization

The Fe_{SAC} and Pt_{NPs}/Fe_{SAC} catalysts were synthesized based on computational guidance. Fe_{SAC} was synthesized through pyrolysis followed

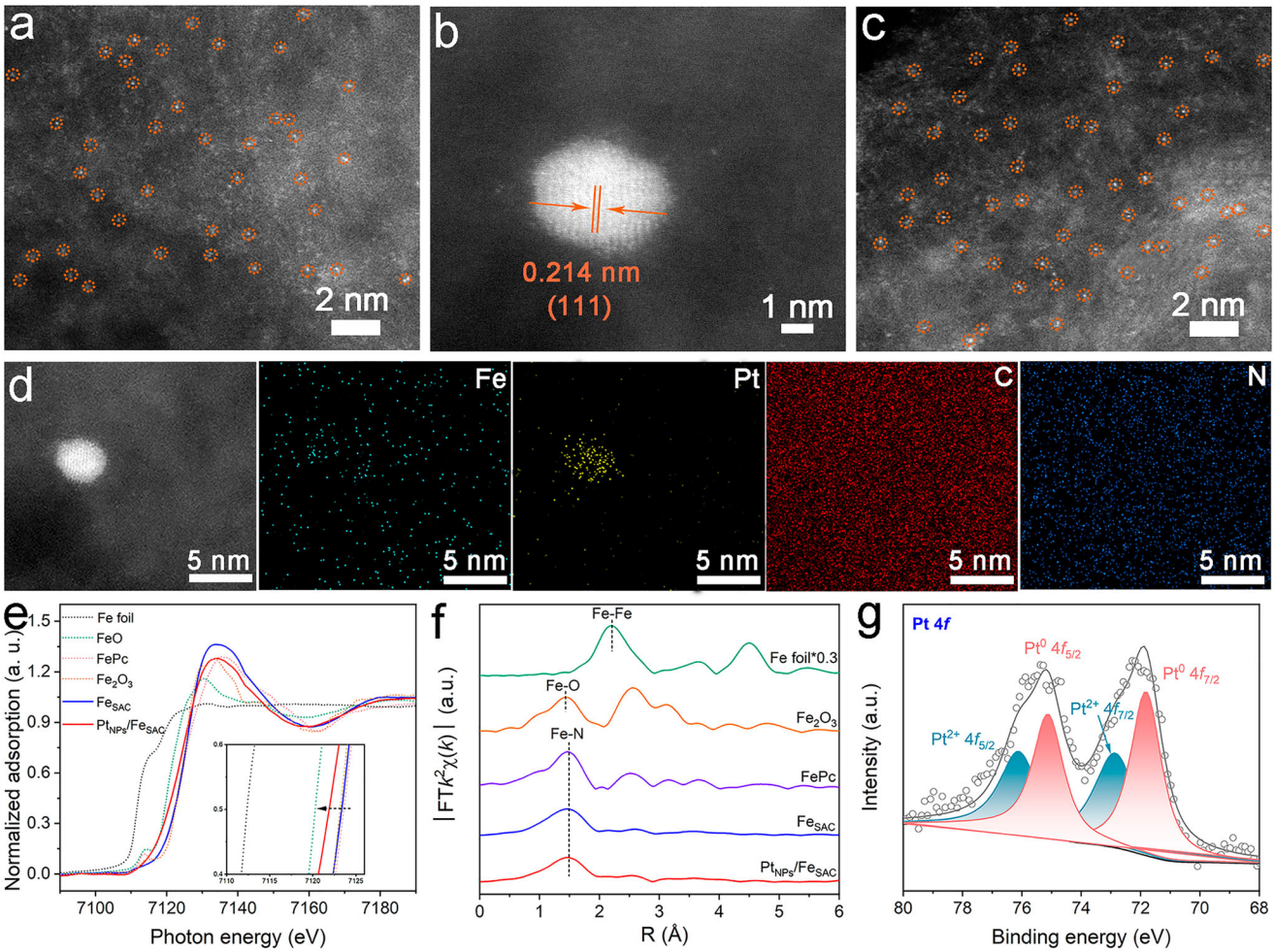

Fig. 3 | Structural characterizations of catalysts. HAADF-STEM images of (**a**) Fe_{SAC} and (**b**, **c**) Pt_{NPs}/Fe_{SAC}. **d** EDX mapping images of Pt_{NPs}/Fe_{SAC}. **e** Fe K-edge XANES spectra of Fe foil, FePc, Fe_2O_3, Fe_{SAC} and Pt_{NPs}/Fe_{SAC}. **f** FT-EXAFS spectra at Fe K-edge. **g** XPS spectrum of Pt_{NPs}/Fe_{SAC} in Pt 4*f* region. Source data are provided as a Source Data file.

by acid etching, while Pt_{NPs} were subsequently loaded onto Fe_{SAC} by a thermal reduction method. High-aberration-corrected high-angle annular dark-field scanning transmission electron microscopy (HAADF-STEM) image of Fe_{SAC} (Fig. 3a) revealed that isolated atomic sites are randomly dispersed on nitrogen doped carbon (NC) without observable metal clusters or particles, consistent with the X-ray diffraction (XRD, Supplementary Fig. 3) result. Inductively coupled plasma optical emission spectrometer (ICP-OES) confirmed a Fe content of 0.66 wt% in Fe_{SAC} (Supplementary Table 1).

In contrast, HAADF-STEM images of Pt_{NPs}/Fe_{SAC} showed Pt_{NPs} with a size of ~3 nm and a lattice distance of 0.214 nm, corresponding to the (111) crystal plane (Fig. 3b). XRD pattern further confirmed the presence of Pt_{NPs} (Supplementary Fig. 3). As illustrated in Fig. 3c, Fe_{SAC} are densely distributed around Pt nanoparticles, and energy dispersion X-ray spectroscopy (EDX, Fig. 3d) mapping confirmed the uniform dispersion of Fe, C, and N elements, with Pt as the primary nanoparticle component. ICP-OES results showed Fe and Pt contents of 0.62 wt% and 0.84 wt%, respectively (Supplementary Table 1).

To investigate the chemical state and atomic structure, X-ray absorption spectroscopy (XAS) and X-ray photoelectron spectroscopy (XPS) were employed. The Fe K-edge X-ray absorption near-edge structure (XANES) spectra revealed that Fe in Fe_{SAC} lies between +2 and +3 oxidation states (Fig. 3e). Notably, Pt incorporation induces a negative shift in the Fe K-edge, indicating a reduced Fe oxidation state, consistent with the theoretical predictions shown in Fig. 1.

Fourier transformed (FT) k^2-weighted extended X-ray absorption fine structure (EXAFS) analysis (Fig. 3f) confirmed the absence of Fe clusters, as FePc, Fe_{SAC} and Pt_{NPs}/Fe_{SAC} exhibited a prominent Fe-N scattering peak at 1.51 Å[33,34]. EXAFS fitting curves revealed that the average coordination numbers of Fe_{SAC} and Pt_{NPs}/Fe_{SAC} are 4.4 and 4.2, respectively, indicating that Fe is coordinated with four nitrogen atoms ($Fe\text{-}N_4$) in both systems. The bond lengths for Fe-N are 1.96 and 1.97 Å, respectively (Supplementary Fig. 4 and Supplementary Table 2). Additionally, wavelet transform (WT) analysis of Fe K-edge EXAFS oscillations (Supplementary Fig. 5) displays a strong signal with a maximum intensity at 3.8 $Å^{-1}$ for Pt_{NPs}/Fe_{SAC}, corresponding to the Fe-N first coordination shell, which is similar to Fe_{SAC}[33]. Impressively, no Fe-Fe signal was detected in WT contour plots for either Fe_{SAC} or Pt_{NPs}/Fe_{SAC}, further confirming the atomically dispersed Fe in both catalysts.

XPS analysis of the Pt 4*f* region (Fig. 3g) showed two Pt^0 peaks at 71.8 ($4f_{7/2}$) and 75.1 eV ($4f_{5/2}$) along with two Pt^{2+} peaks at 72.7 ($4f_{7/2}$) and 76.0 eV ($4f_{5/2}$) in Pt_{NPs}/Fe_{SAC} (Fig. 2g), likely due to partial surface oxidation or electron donation from adjacent Fe atoms[35,36]. The successful synthesis and characterization of Pt_{NPs}/Fe_{SAC} confirmed its distinct structural features, including reduced Fe oxidation states upon Pt incorporation and stable $Fe\text{-}N_4$ coordination.

In situ spectroscopy

To demonstrate the cascade reaction mechanism during the dynamic catalytic process of NORR in the Pt_{NPs}/Fe_{SAC} dual-site catalyst, in situ

https://doi.org/10.1038/s41467-025-63365-7

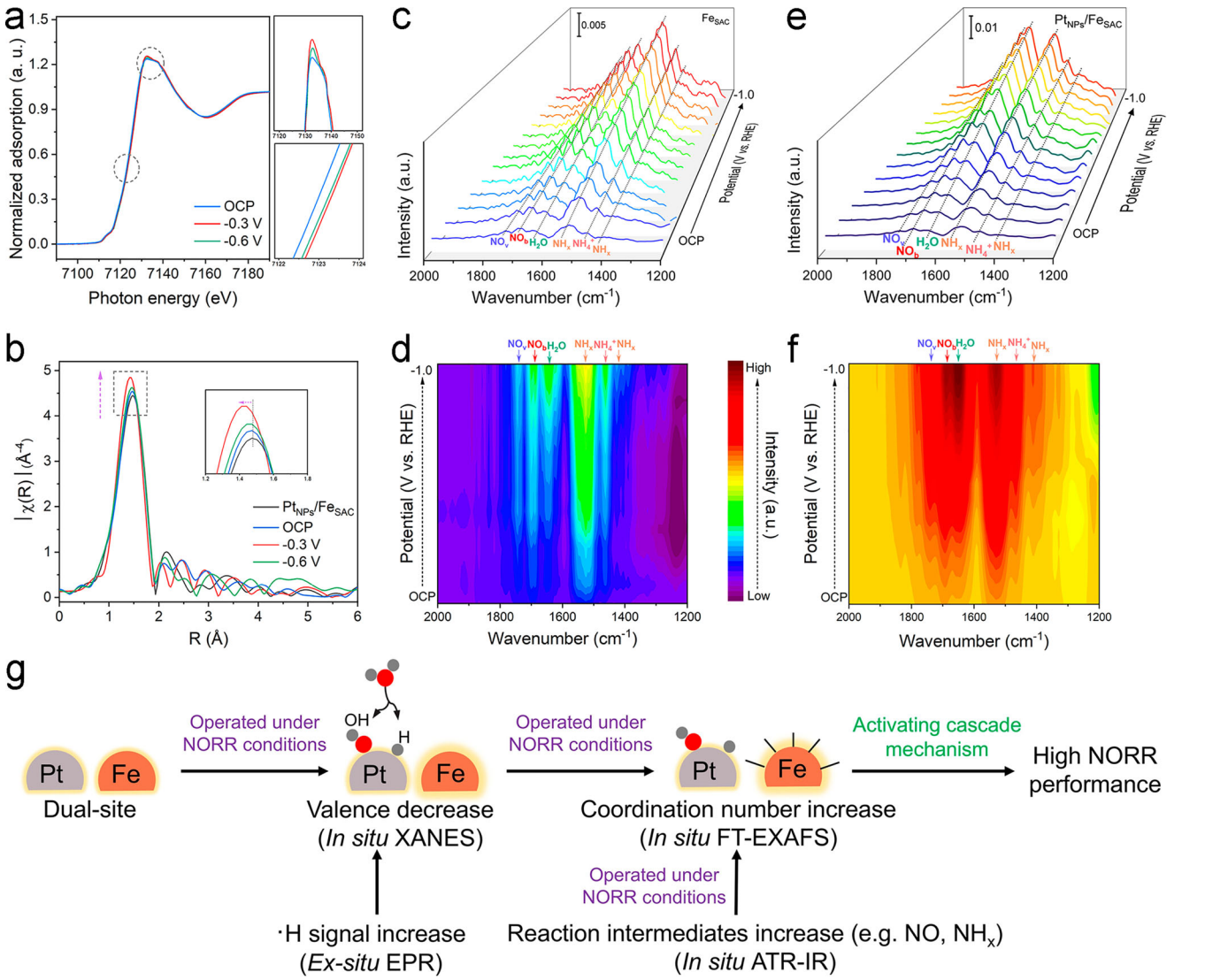

Fig. 4 | In situ XAS and ATR-IR spectra of NORR. a In situ Fe K-edge XANES spectra of Pt_{NPs}/Fe_{SAC} at different potentials (without iR-correction). (Inset) Magnified white-line peak and pre-edge XANES region. **b** Corresponding FT-EXAFS spectra at Fe K-edge (without iR-correction). Potential-dependent in situ ATR-IR spectra of (**c**) Fe_{SAC} and (**e**) Pt_{NPs}/Fe_{SAC} (without iR-correction). Corresponding 2D ATR-IR contour map of (**d**) Fe_{SAC} and (**f**) Pt_{NPs}/Fe_{SAC} (without iR-correction). **g** Reaction mechanisms. Source data are provided as a Source Data file.

electrochemical XAS and attenuated total reflection-infrared (ATR-IR) spectroscopies were conducted. As shown in Fe K-edge XANES spectra of Pt_{NPs}/Fe_{SAC} (Fig. 4a), the white-line peak intensity increased as the applied potential decreases from open circuit potential (OCP) to −0.3 V, indicating that NO adsorption on Fe sites leads to an increase in coordination number. A shift of the adsorption edge to higher energy suggested an increased oxidation state of Fe. As the potential further decreased to −0.6 V, the white-line peak intensity diminished, implying NO consumption and reduction of Fe valence state, confirming Fe_{SAC} as the real active sites.

The EXAFS spectra (Fig. 4b) further revealed the dynamic evolution of Fe's local coordination. The Fe-N peak was enhanced with decreasing the applied potentials, suggesting that the intermediates adsorb on Fe sites. A notable negative shift from OCP to −0.3 V, suggested the formation of a shorter Fe-N bond due to NO adsorption. When the potential was further reduced to −0.6 V, the peak moved from 1.53 to 1.58 Å, signaling the occurrence of NORR and aligning well with the XANES results.

Next, in situ ATR-IR spectroscopy was employed to identify the adsorbed intermediates. As shown in Figs. 4c and 4e, both Fe_{SAC} and Pt_{NPs}/Fe_{SAC} display peaks corresponding to NO adsorption, including vertical mode (NO_v) and bent mode NO_b)[22,37]. Specifically, for Fe_{SAC}, the NO_v and NO_b peaks were observed at 1743.4 and 1694.5 cm^{-1}, respectively. Similarly, in the spectra of Pt_{NPs}/Fe_{SAC}, the NO_v and NO_b peaks appeared at 1743.3 and 1693.2 cm^{-1}, respectively. No significant peak shift was observed, suggesting NO molecule was adsorbed on the similar active site in both catalysts. As shown in Supplementary Fig. 9, the Pt nanoparticles supported on NC (Pt_{NPs}) exhibits only a strong H_2O adsorption peak under a 1.0 vol% NO/Ar atmosphere, which indicates that the Fe single atom site remains the primary adsorption site for NO in Pt_{NPs}/Fe_{SAC}. Besides, the adsorption energies of NO on Fe sites and Pt sites were systematically evaluated. For Pt sites, two distinct adsorption configurations (Supplementary Fig. 10b,c) were analyzed, revealing positive adsorption free energies of 0.36 eV and 0.53 eV, respectively. In contrast, the adsorption energy of NO on Fe site was determined to be −1.36 eV (Supplementary Fig. 10a). These results strongly suggest that NO has a significantly higher affinity for Fe site than for Pt site.

Impressively, the higher intensity of these peaks in Pt_{NPs}/Fe_{SAC} indicated stronger NO adsorption. With the potentials shifted from

OCP to −1.0 V, the intensity of NO_b peak increased, suggesting effective NO activation at Fe sites. As illustrated in Figs. 4d and 4f, the NO_b peak intensity in Pt_{NPs}/Fe_{SAC} spectra is much stronger than that of Fe_{SAC}, implying that the lower valence state of Fe site induced by introduction of Pt nanoparticles is more conducive to activate NO, in agreement with the DFT results shown in Figs. 1 and 2. The NO temperature-programmed desorption (NO-TPD) measurement was conducted to evaluate the NO adsorption capability. In Supplementary Fig. 11, the NO chemisorption peak for Fe_{SAC} appeared at 247.2 °C, while that of Pt_{NPs}/Fe_{SAC} was observed at a higher temperature of 266.8 °C. The elevated desorption temperature indicates stronger NO adsorption on Pt_{NPs}/Fe_{SAC}, suggesting that the introduction of Pt nanoparticles enhances the NO binding affinity.

Compared to Fe_{SAC}, the peak of -OH bending vibration at 1648 cm^{-1} was strengthened in Pt_{NPs}/Fe_{SAC} spectra, indicating that the Pt nanoparticles facilitate H_2O electrolysis to produce *H, which is beneficial for subsequent NO hydrogenation (Figs. 4d, f)[38,39]. This was further verified by the electron paramagnetic resonance (EPR) and H_2-TPD techniques[40–43]. As shown in Supplementary Fig. 12, the Pt_{NPs}/Fe_{SAC} and Fe_{SAC} were electrolyzed in Ar-saturated 0.5 M K_2SO_4 electrolyte for 10 min at −0.6 V and −0.7 V respectively, and then the EPR tests were conducted immediately. The distinct hydrogen radical signals were detected for Pt_{NPs}/Fe_{SAC} but not in Fe_{SAC}, which confirmed that the introduction of Pt nanoparticles facilitated the electrochemical generation of hydrogen radicals. However, when the Pt_{NPs}/Fe_{SAC} was tested in NO-saturated 0.5 M K_2SO_4 electrolyte for 10 min at −0.6 V, the signal of hydrogen radicals disappeared, proving that the hydrogen radicals were involved in the NORR reaction (Supplementary Fig. 13). Besides, H_2-TPD experiments were also carried out to investigate the hydrogen spillover effect. The H_2 desorption peak of Pt_{NPs}/Fe_{SAC} (303.4 °C) exhibited a positive shift compared to that of Fe_{SAC} (274.3 °C), indicating a stronger binding strength between hydrogen and Pt_{NPs}/Fe_{SAC} catalyst (Supplementary Fig. 14). This finding implies that the presence of Pt nanoparticles increases the hydrogen concentration around the Pt sites, thereby triggering the hydrogen spillover effect that facilitates the NO hydrogenation[43]. Hydrogenated intermediates NH_x (1412 and 1530 cm^{-1}) were progressively formed at lower potentials, ultimately converting to NH_4^+ (1465 cm^{-1})[44–46]. Moreover, when Pt_{NPs}/Fe_{SAC} was tested under Ar atmosphere, only a strong peak corresponding to H_2O was observed, confirming the signals of hydrogenated intermediates derive from NO (Supplementary Fig. 15). Overall, these results clearly demonstrated Pt_{NPs} served as electron donors, increasing Fe site electron density to enhance NO adsorption while simultaneously promoting water dissociation to supply protons for efficient NORR. These results clearly demonstrated that a cascade reaction mechanism occurs on the dual-site catalyst, Pt_{NPs}/Fe_{SAC}, thereby promoting NORR (Fig. 4g).

NORR performance evaluation

The NORR performance was evaluated in 0.5 M K_2SO_4 electrolyte, using an air-tight H cell. Prior to electrolysis, high-purity Ar was purged into the electrolyte to remove residual oxygen. As shown in Fig. 5a, the linear sweep voltammetry (LSV) curves revealed a significant increase in current density for Pt_{NPs}/Fe_{SAC} in 1 vol% NO atmosphere compared to Ar-saturated conditions, confirming effective NO reduction on the catalyst surface. Compare to Fe_{SAC}, Pt_{NPs} and NC, the Pt_{NPs}/Fe_{SAC} showed the largest current density gap, indicating superior NORR activity (Supplementary Fig. 16).

As depicted in Fig. 5b, the NH_3 yield rate and FE of Pt_{NPs}/Fe_{SAC} increase steadily with applied potentials from -0.4 to -0.6 V, reaching the maximum values of 709.7 μg h^{-1} $mg_{cat.}^{-1}$ and 90.3% at −0.6 V, outperforming previously reported NORR catalysts (Supplementary Table 4). NH_3 quantification via colorimetric method (Supplementary Fig. 17) and nuclear magnetic resonance (NMR) spectroscopy (Supplementary Fig. 18) yielded consistent results, ensuring measurement accuracy (Supplementary Fig. 19). However, at the applied potentials beyond −0.6 V, NORR performance of Pt_{NPs}/Fe_{SAC} declined due to the competing HER (Supplementary Fig. 20). Other liquid byproducts such as N_2H_4 and NH_2OH were not detected (Supplementary Figs. 21 and 22). In comparison, Fe_{SAC} obtained its highest NORR performance at -0.7 V with a NH_3 yield of 444.2 μg h^{-1} $mg_{cat.}^{-1}$ and FE of 56.6% (Fig. 5c and Supplementary Fig. 23), while Pt_{NPs}/NC and bare NC exhibited negligible NORR activity (Fig. 5c).

As shown in Supplementary Fig. 26, Pt_{NPs}/Fe_{SAC} exhibits a significantly higher NH_3 partial current densities than Fe_{SAC}, which confirms the superior intrinsic activity of Pt_{NPs}/Fe_{SAC} towards NORR. We also conducted electrochemical NORR tests under 10 vol% NO/Ar to explore the mechanistic origin of the activity enhancement. In Supplementary Fig. 27, the Pt_{NPs}/Fe_{SAC} achieved an enhanced NH_3 yield rate of 1562.9 μg h^{-1} $mg_{cat.}^{-1}$ and FE of 92.3% under 10 vol% NO/Ar compared to 1.0 vol% NO/Ar condition. The remarkable improvement in performance primarily originates from an acceleration of the NO adsorption step rather than solely the intrinsic catalytic activity, indicating the mass transport and surface NO availability are important limiting factors under lower concentrations. In addition, the turnover frequency (TOF) values of Fe_{SAC} and Pt_{NPs}/Fe_{SAC} are 194.2 h^{-1} and 344.2 h^{-1}, respectively, under 1.0 vol% NO/Ar atmosphere. The significantly enhanced TOF value suggests that the Pt nanoparticle introduction facilitates a quick water dissociation and thereby accelerates the turnover frequency of the NO reduction sites.

DFT and in-situ electrochemical experiments clearly verified that Pt_{NPs} served as electron donors, increasing the electron density at the Fe single-atom site to promote NO adsorption, while facilitating water dissociation for proton supply and promoting NO hydrogenation. This dual role enabled efficient NO-to-NH_3 conversion with high activity and selectivity by activating the cascade reaction mechanism.

To validate that NH_3 originated from NO reduction, control experiments were conducted under three conditions: (1) electrolysis at −0.6 V in Ar-saturated electrolyte, (2) testing at OCP in NO-saturated electrolyte, and (3) testing in NO-saturated electrolyte with bare carbon paper (CP) as work electrode (Fig. 5d). Only negligible NH_3 was detected in these cases, confirming that NH_3 formation on Pt_{NPs}/Fe_{SAC} exclusively results from NO reduction. Additionally, an isotope labeling experiment was performed to exclude the possibility of nitrogen contamination. The laboratory-produced ^{15}NO was used as the feeding gas for NORR at −0.6 V for 1 h. As shown in Fig. 5e, the NMR analysis conclusively verified that the generated NH_3 is originated from NO.

Electrocatalyst stability is crucial for long-term energy conversion and storage. Pt_{NPs}/Fe_{SAC} demonstrated excellent durability, maintaining stable NH_3 yield and FE over ten consecutive cycles (Fig. 5f). A long-term stability test (>70 h, Supplementary Fig. 30) showed no significant decline in current density, further confirming its robust electrochemical stability. Post-reaction characterization revealed minor catalyst changes: XRD pattern showed weakened Pt diffraction peaks, suggesting partial Pt dissolution (Supplementary Fig. 31). ICP analysis detected trace amounts of Pt in the electrolyte post-NORR (Supplementary Table 3). XANES analysis exhibited a slight increase in Fe valence state after NORR test (Supplementary Fig. 32a). EXAFS spectra revealed no Fe-Fe bond formation, confirming Fe remains atomically dispersed (Supplementary Fig. 32b). XPS spectrum of Pt exhibited two dominant peaks at 72.1 and 74.8 eV, which were attributed to Pt^0 $4f_{7/2}$ and Pt^0 $4f_{5/2}$, respectively, indicating that a small amount of Pt oxide species on the catalyst surface were reduced (Supplementary Fig. 33).

To mitigate NO mass transport limitations due to its low solubility (-1.92 mmol L^{-1} atm^{-1} in water at 25 °C), NORR was conducted in a membrane electrode assembly (MEA) electrolyzer (Supplementary Fig. 34)[47,48]. Compared to H-cell, the MEA significantly enhanced current density, suggesting improved NO utilization (Fig. 5g). As shown in Fig. 5h, increasing the applied cell voltage from 1.2 to 1.6 V *vs.* cell

https://doi.org/10.1038/s41467-025-63365-7

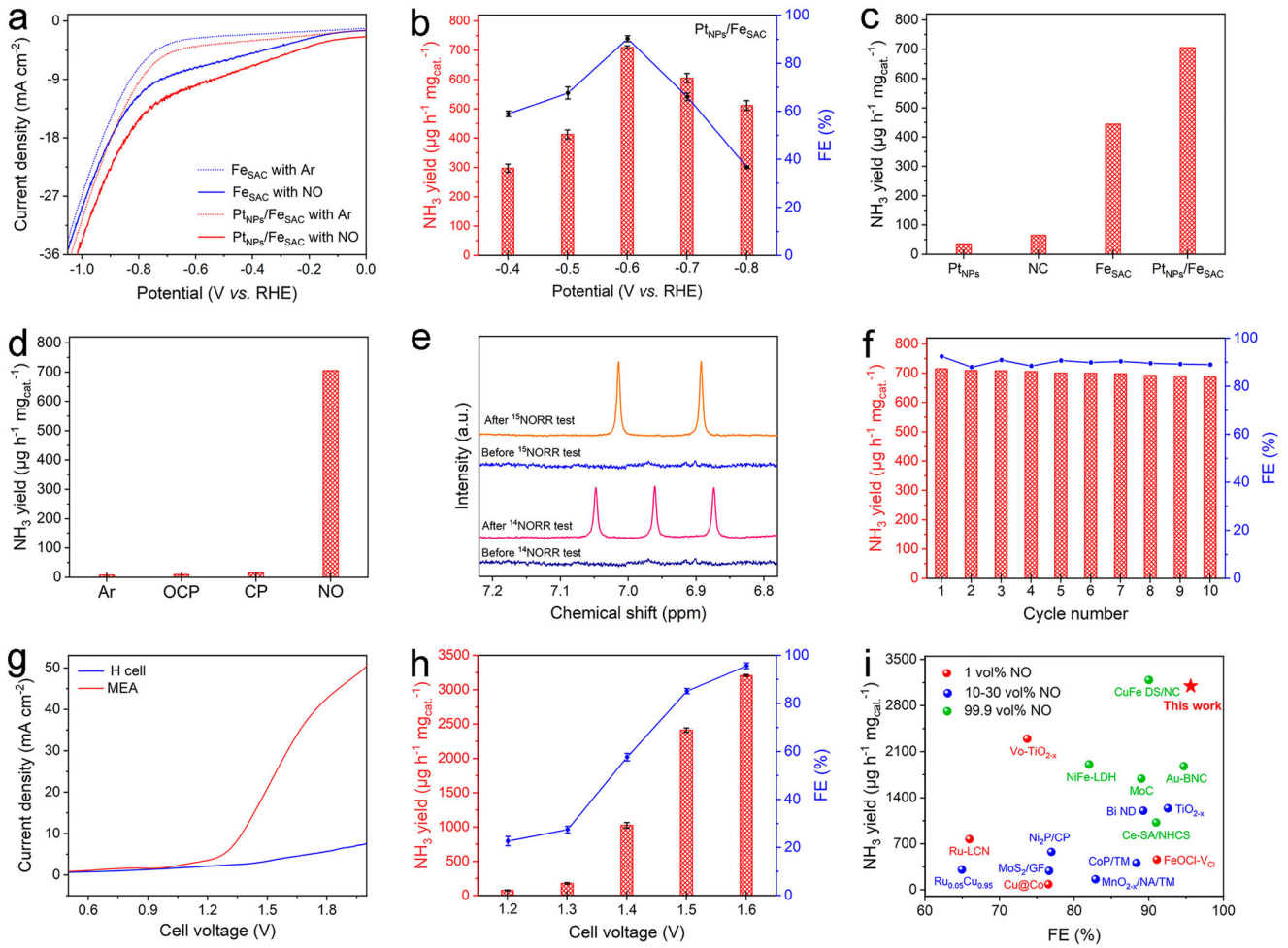

Fig. 5 | Electrochemical NORR performance. a LSV curves of Fe_{SAC} and Pt_{NPs}/Fe_{SAC} in Ar- and 1 vol% NO-saturated 0.5 M K_2SO_4 (pH =7.1, without iR-correction) at scan rate of 10 mV s^{-1}. **b** NH_3 yield and FE with 1 vol% NO over Pt_{NPs}/Fe_{SAC} at each given potential (without iR-correction). **c** The NH_3 yield of Pt_{NPs}, NC, Fe_{SAC} and Pt_{NPs}/Fe_{SAC}. **d** NH_3 yield of Pt_{NPs}/Fe_{SAC} under different conditions. **e** ^{1}H NMR spectra of the electrolyte fed by ^{15}NO and ^{14}NO for NORR over the Pt_{NPs}/Fe_{SAC} at −0.6 V (without iR-correction). **f** NORR cycling stability test over the Pt_{NPs}/Fe_{SAC} at −0.6 V (without iR-correction). **g** LSV curves of Pt_{NPs}/Fe_{SAC} test in MEA electrolyzer and H cell at scan rate of 10 mV s^{-1} (without iR-correction). **h** Corresponding NH_3 yield and FE of Pt_{NPs}/Fe_{SAC} (without iR-correction). **i** Comparison of NORR performance with other electrocatalysts. Error bars indicate the relative standard deviations of the mean ($n = 3$). Source data are provided as a Source Data file.

voltage leads to higher NH_3 yield and FE. Notably, Pt_{NPs}/Fe_{SAC} achieved the high NH_3 yield of 3207.7 μg h^{-1} $mg_{cat.}^{-1}$ and FE of 95.6% at 1.6 V *vs.* cell voltage (Fig. 5h), surpassing all previously reported NORR catalyst even tests under high NO concentration (Fig. 5i).

To explore alternative metal nanoparticles, Au_{NPs}/Fe_{SAC} was synthesized for NO-to-NH_3 conversion. TEM images (Supplementary Fig. 35) and XRD patterns (Supplementary Fig. 36) clearly verified that successful Au nanoparticle deposition. The obtained Au_{NPs}/Fe_{SAC} achieved optimal NH_3 yield of 595.4 μg h^{-1} $mg_{cat.}^{-1}$ and FE of 78.9% at -0.5 V, further demonstrating the versatility of metal-modified Fe_{SAC} systems (Supplementary Fig. 37).

In summary, we present an electron-donating particle-mediated strategy that integrates Pt_{NPs} as the electron donor into the Fe_{SAC} electrocatalyst to construct dual-active-site architectures, thereby enhancing NO adsorption while promoting water dissociation and NO hydrogenation for significantly improving neutral NORR at low NO concentration (1 vol%). In situ spectro-electrochemical experiments, coupled with theoretical calculations, confirmed that the Pt nanoparticles serve as electron donors, increasing the electron density at the Fe single-atom site to promote NO adsorption, while facilitating water dissociation to provide protons and thus reducing the activation energy of NO hydrogenation. The synergistic interplay between these dual sites enables a cascade reaction mechanism achieving a superior NORR performance with a NH_3 FE up to 90.3% and a high NH_3 yield rate of 709.7 μg h^{-1} $mg_{cat.}^{-1}$ under 1 vol% NO concentration at −0.6 V, outperforming Fe_{SAC} (NH_3 yield rate: 444.2 μg h^{-1} $mg_{cat.}^{-1}$, FE: 56.6%) and prior to systems operating under high NO concentrations. Notably, in a MEA electrolyzer, the system achieved the NH_3 yield of 3207.7 μg h^{-1} $mg_{cat.}^{-1}$. This work not only offers an attractive earth-abundant nanocatalyst for NH_3 electrosynthesis at low NO concentrations, but also provides an innovative methodology for designing superior electrocatalytic NORR systems through a dual-active-site strategy, paving the way for large scale NH_3 electrosynthesis.

Methods

Chemicals

Ketjen black ecp600JD (KJ), Nafion and carbon paper (CP) were purchased from Suzhou Sinero Thechology Co., Ltd (Suzhou, China). Sodium hydroxide (NaOH, A. R. grade), sodium nitrite ($NaNO_2$, A. R. grade), p-aminobenzenesulfonic acid (pAA, $C_6H_7NO_3S$, A. R. grade) m-phenylenediamine (mPDA, $C_6H_8N_2$, 99.5%) ammonium persulfate ($(NH_4)_2S_2O_8$, A. R. grade), iron chloride hexahydrate ($FeCl_3{\cdot}6H_2O$, 99%), polyvinylpyrrolidone (PVP, Mw24000), sodium hypochlorite (NaClO, 6–14% active chlorine basis) and ethylene glycol (EG, A. R. grade) were obtained from Aldrich Chemical Reagent Co., Ltd. (Shanghai, China). Chloroplatinic acid hexahydrate ($H_2PtCl_6{\cdot}6H_2O$, A. R. grade), gold

chloride trihydrate ($HAuCl_4{\cdot}3H_2O$, A. R. grade), salicylic acid ($C_7H_6O_3$, A. R. grade), trisodium citrate dihydrate ($Na_3C_6H_5O_7{\cdot}2H_2O$, A. R. grade), sodium nitroferricyanide (III) dihydrate ($Na_2Fe(CN)_5NO{\cdot}2H_2O$, A. R. grade), dimethyl sulfoxide (DMSO-*d6*, 99.9%), ammonium chloride ($^{14}NH_4Cl$, A. R. grade; $^{15}NH_4Cl$, 99atom %), sodium borohydride ($NaNH_4$, A. R. grade) and sodium nitrite ($Na^{15}NO_2$, 99atom %) were bought from Macklin Chemical Reagent Co., Ltd. (Shanghai, China). Fe powder (99.9%), potassium thiocyanate (KSCN, A. R. grade) and hydrochloric acid (HCl, A. R. grade) were supplied by Sinopharm Chemical Reagent Co., Ltd. (Shanghai, China). All the reagents were used as received. The water used throughout all experiments was purchased from Wahaha Group Co., Ltd. (Hangzhou, China).

Preparation of NC

1.0 g of KJ was dispersed in 30 mL H_2O and sonicated in an ice bath for 2 h to labeled A1. Separately, 0.74 g pAA was dissolved in 30 mL H_2O. To this solution, 9 mL of 1 M NaOH, 4 mL of 1 M $NaNO_2$ and 21 mL of 1 M HCl were added to prepare the diazo salt (labeled A2), maintain the reaction at 0 °C. Subsequently, the A2 was mixed with A1. To initiate surface grafting of the diazonium salt, 0.7 g of reduced Fe powder was introduced. Afterward, 25 mL concentrated HCl, 7.6 g of mPDA, 23 mL of 1 M $FeCl_3$ and 70 mL of 2 M $(NH_4)_2S_2O_8$ solution were added, and the reaction was allowed to react overnight. After filtration, the product was washed with water for 3 times and vacuum drying overnight to yield the NC precursor.

Preparation of Fe_{SAC}

0.6 g of the NC precursor was ultrasonically dispersed in 30 mL H_2O, followed by the addition of 1.8 mL of 1 M $FeCl_3$ and 6 mL of 1 M KSCN. The solvent was removed by rotary evaporation, and the residue was heated to 950 °C for 1 h under an Ar atmosphere. The obtained black powder was dispersed in 50 mL of 1 M HCl solution overnight at 80 °C. Then, the powder was washed with water 3 times, and drying overnight. Finally, the dried powder was heated at 950 °C for 3 h in an Ar atmosphere to yield Fe_{SAC}.

Preparation of Pt_{NPs}/Fe_{SAC}

100 mg Fe_{SAC} was dispersed in 20 mL of EG. Next, 5 mg $H_2PtCl_6{\cdot}6H_2O$ was dispersed in 20 mL of EG and then dripped into Fe_{SAC}. The obtained suspension was stirred for 2 h at room temperature and then treated at 160 °C for 90 min. Afterward, the final product was washed 3 times and dried overnight. The Pt_{NPs} was synthesized by replacing the Fe_{SAC} to NC.

Preparation of Au_{NPs}/Fe_{SAC}

100 mg of Fe_{SAC} and 10 mg of PVP were dispersed in 30 mL H_2O. Then, 400 µL of a 10 mg/mL $HAuCl_4$ solution was added dropwise, followed by 100 mg of $NaNH_4$ dissolved in 20 mL H_2O to reduce $HAuCl_4$. The mixture was stirred for 10 min at room temperature.

Preparation of work electrodes

10 mg catalyst powder was dispersed in 950 µL ethanol and 50 Nafion mixture by sonication for 2 h. Next, 100 homogenous ink was dropped on CP (1*1 cm^2) and dried at room temperature. The catalyst loading is 1 mg cm^{-2}.

Characterizations

XRD patterns were collected by a LabX XRD-6100 X-ray diffractometer with Cu Kα radiation (40 kV, 30 mA) of wavelength 0.154 nm (SHIMADZU, Japan). TEM images were acquired on a Hitachi H-8100 electron microscopy (HITACHI, Japan), equipped with EDS mapping. XPS measurements were conducted on an ESCALABMK II X-ray photoelectron spectrometer using Mg as the exciting source. In situ electrochemical ATR-FTIR spectra were obtained by using a Thermo iS50. The XAS spectra were performed at the BL11B beamline of Shanghai Synchrotron Radiation Facility (SSRF). The incident photons were monochromatized by a Si (111) double-crystal monochromator. The absorbance data of spectrophotometer were measured on SHIMADZU UV-1800 ultraviolet-visible (UV-Vis) spectrophotometer.

Electrochemical measurements

Firstly, the Nafion 211 membrane was protonated in 5 wt% H_2O_2 at 80 °C for 1 h, then treated in 0.5 M H_2SO_4 for 3 h, and finally soaked in water for 6 h. All steps were performed at 80 °C. Electrochemical measurements were performed with a CHI660E electrochemical station (CH Instruments, Inc., Shanghai) in a H-cell under ambient condition, which was separated by Nafion 211 membrane. All the NORR tests were conducted in 0.5 M K_2SO_4 electrolyte (30 mL, pH = 7.1), which was stored at room temperature. The Pt_{NPs}/Fe_{SAC}, Ag/AgCl and graphite rod acted as the working electrode (WE), reference electrode (RE) and counter electrode (CE), respectively. The reference electrode was calibrated to the reversible hydrogen electrode (RHE) scale in all measurements using the following equation:

$$E(\mathrm{RHE}) = E(\mathrm{Ag/AgCl}) + (0.059 \times \mathrm{pH} + 0.197)\mathrm{V} \quad (1)$$

All data are presented without iR-correction. High purity Ar gas (99.999%) was bubbled into cathode chamber with the flow rate of 30 sccm for 30 min to removal oxygen before NORR. Then, the low-concentration NO (1% v/v) was firstly washed by 4 M KOH and then fed at 30 sccm for 30 min to saturate the electrolyte, maintain a constant flow during the electrochemical tests. The electrocatalytic NORR measurements were conducted at different potentials for 1 h, and then the electrolyte was collected and analysed. For NORR tested in MEA, a piece of anion exchange membrane (AEM, Sustainion, thickness: 50 µm) was used to separate cathode and anode chambers. Before electrochemical test, the AEM was immersed in 1 M KOH for 12 h, then rinsed with deionized water, and finally stored in pure water. The RuO_2 supported on nickel foam (RuO_2/NF) as anode tested in 1 M KOH (30 mL, pH = 14), while Pt_{NPs}/Fe_{SAC} was used as the cathode for NORR and the tail gas was absorbed by 1 M HCl. The error bars were the mean values standard deviation according to the obtained data. All experiments were carried out at room temperature (≈25 °C).

Determination of NH_3

The produced NH_3 was quantified by the indophenol blue method[49] and NMR. For indophenol blue method, standard NH_3 solution with a series of concentrations were used to calibrated the concentration-absorbance curves. The fitting curve ($y = 0.3435x + 0.05843$, $R^2 = 0.9999$) showed good linear relation of absorbance value with NH_3 concentration. All electrolytes were diluted 10 times before testing unless otherwise specified. For ^1H NMR measurements, the electrolyte after electrolysis was diluted 2 times with 1 M HCl to adjust the pH to acidic. Then, 100 mL DMSO-d6 was added in 500 µL acidified electrolyte.

Determination of FE and Yield of NH_3

The FE for NH_3 synthesis was calculated as the amount of electric charge used for NH_3 production divided by the total charge passed through the electrodes during electrolysis. The total amount of NH_3 produced was measured using colorimetric methods. The FE could be calculated as follows:

$$\mathrm{FE}(NH_3) = 5 \times F \times [NH_3] \times V/(17 \times Q) \times 100\% \quad (2)$$

NH_3 yield was calculated using the following equation:

$$NH_3\mathrm{yield} = [NH_3] \times V/(m_{cat.} \times t) \quad (3)$$

where F is the Faraday constant (96485 C/mol), [NH_3] is the measured NH_3 concentration, V is the volume of the electrolyte in the cathodic chamber, Q is the total quantity of applied electricity, t is the reduction time, $m_{cat.}$ is the loaded mass of catalyst on carbon paper.

Determination of FE and yield of gas byproducts

The gas products (N_2O, N_2 and H_2) were quantified on a Gas chromatography (GC 2014 SHIMADZU). The yield and FE of gas products were calculated according to the following equations:

$$r_{gas} = P_{gas} \times F_{gas} \times 3.6 \times 10^6 / (m_{cat.} \times V_m) \quad (4)$$

$$FE_{gas} = n_{gas} \times r_{gas} \times t \times m_{cat.} \times F \times 10^{-6} / Q \times 100\% \quad (5)$$

Where r_{gas} is the gas product formation rate, P_{gas} is the percentage of gas in the total gas flow detected by GC, F_{gas} is the flow rate of 1 vol% NO/Ar, $m_{cat.}$ is the loaded mass of catalyst on carbon paper, V_m is the molar volume in the standard condition (V_m = 22.4 L/mol), n_{gas} is the electron transfer numbers of gas product, t is the reduction time, F is the Faraday constant (96485 C/mol), Q is the total quantity of applied electricity.

TOF calculations

We calculate the TOF according to the following equation:

$$TOF(h^{-1}) = \frac{I_{product}/nF}{m_{cat.} \times \alpha / M_{metal}} \times 3600 \quad (6)$$

Where $I_{product}$ is partial current for NH_3, n is number of electrons transferred for NH_3, F is Faradaic constant, $m_{cat.}$ is catalyst mass in the electrode, α is mass ratio of active atoms in catalysts, M_{metal} is atomic mass of metal.

Electrochemical in situ ATR-IR measurements

The in situ electrochemical ATR-IR measurements were conducted on a Nicolet iS50 FT-IR spectrometer with a liquid nitrogen-cooled MCT-A detector. The Si prism loaded with catalyst, Pt plate and Ag/AgCl were used as the working electrode, counter electrode and reference electrode, respectively, with 0.5 M K_2SO_4 as electrolyte. During the process of tests, 1 vol% NO was bubbled into the electrolyte with the flow rate of 10 sccm. Prior to testing, the Si prism was coated with Au film. The Si prism was first polished by 100 nm Al_2O_3. Next, the Si prism was soaked in a piranha solution for 30 min to removal organic contaminants. Then, the reflecting surface was immersed in a mixture of the Au plating solution (5.75 mM $NaAuCl_4 \cdot 2H_2O$ + 0.025 M NH_4Cl + 0.075 M Na_2SO_3 + 0.025 M $Na_2S_2O_3$ + 0.026 M NaOH) and a 2 wt % HF solution at 60 °C for 5 min. Afterward, the Au film was rinsed with deionized water and dried with N_2. In situ ATR-IR spectra were collected at OCP and different applied potentials.

Electrochemical in situ XAS measurements

The in situ XAS measurements were conducted in the fluorescence mode using a home-made electrochemical cell. The Pt_{NPs}/Fe_{SAC}, Ag/AgCl and graphite rod were used as working electrode, reference electrode and counter electrode, respectively. Prior to NORR test, 30 mL 0.5 M K_2SO_4 electrolyte was added into electrochemical cell and purged with Ar gas to removal dissolved oxygen. Subsequently, 1.0 vol % NO was bubbled through the deoxygenated electrolyte for 30 min to ensure saturation. Finally, the XAS spectra were recorded at OCP and different applied potentials.

Computation and model details

All spin-polarized simulations were carried out using density functional theory as implemented in the GPAW software[50,51] version 19.8.1. The exchange-correlation effects were accounted for using the BEEF-vdW-functional, which combines the generalized gradient approximation with the Langreth-Lundqvist van der Waals-functional to achieve accurate adsorption energies. A 2 × 2 × 1 k-point mesh was used because it ensures energy convergence in the calculation (Supplementary Fig. 38). The vacuum layer thickness of 25 Å was employed in the modeling framework (Supplementary Fig. 39). Then, to model the solvent at the electrochemical interface, a hybrid implicit/explicit approach was employed in the vacuum layer, where 40 explicit water molecules surrounded the electrode surface, and the remaining water was modeled using the SCMVD[52] dielectric continuum model. The positions and orientations of the explicit water molecules were optimized using the minima hopping global optimization method[53] as implemented in ASE[54]. To simulate the nanoparticle environment, nine Pt atoms were introduced into the FeN_4 structure.

To investigate NORR electrocatalytic processes involving proton-coupled electron transfer, free energy calculations were performed using the computational hydrogen electrode (CHE) approach. The chemical potential (the free energy per H) for H* + e was correlated with that of $1/2H_2$[55]. The free energies of the reaction intermediates were defined as by $\Delta G = \Delta E + \Delta ZPE - T\Delta S$, where ΔE, ΔZPE, T, and ΔS represent the reaction energy, zero-point energy, temperature (298.15 K), and the entropy, respectively (Supplementary Table 5 and 6). The optimized computational models are provided in Supplementary Data 1.

Enhanced sampling

The slow growth sampling approach[56,57] in the constrained molecular dynamics simulation method can be used to describe the kinetic energy barrier in the reaction process by setting a suitable collective variable (CV, ξ), which changes from state 1 to state 2 at a certain transformation rate $\dot{\xi}$. The work performed throughout the entire process from state 1 to state 2 can be calculated using the following formula:

$$w_{state1 \to state2} = \int_{\xi(state1)}^{\xi(state2)} \left(\frac{\partial V(q)}{\partial \xi} \right) \cdot \dot{\xi} \, dt \quad (7)$$

Where $V(q)$ represents the free energy, and $\frac{\partial V(q)}{\partial \xi}$ is calculated using the SHAKE algorithm. When approaching the infinitesimal limit $\dot{\xi}$, the work $w_{state1 \to state2}$ required from state 1 to state 2 corresponds to the difference in free energy. In the SG sampling method, $\partial\xi$ is selected to 0.0005 Å, and the final reaction's free energy barrier can be obtained by aggregating the free energy distribution diagram.

Data availability

Full data supporting the findings of this study are available within the article and its Supplementary Information, as well as from the corresponding author upon reasonable request. Source data are provided with this paper. The CIF files of computationally optimized structures are freely accessible on the website at https://github.com/sunyao-coder/Structures. Source data are provided with this paper.

References

1. Buttignol, F. et al. Iron-catalysed cooperative redox mechanism for the simultaneous conversion of nitrous oxide and nitric oxide. *Nat. Catal.* **7**, 1305–1315 (2024).
2. Ghosh, P. et al. Get to Know NO. *Nat. Chem.* **16**, 1382 (2024).
3. Hwang, J. et al. Regulating oxygen activity of perovskites to promote NO_x oxidation and reduction kinetics. *Nat. Catal.* **4**, 663–673 (2021).
4. Anenberg, S. et al. Impacts and mitigation of excess diesel-related NO_x emissions in 11 major vehicle markets. *Nature* **545**, 467–471 (2017).
5. Han, L. et al. Selective catalytic reduction of NO_x with NH_3 by using novel catalysts: state of the art and future prospects. *Chem. Rev.* **119**, 10916–10976 (2019).

6. He, G. et al. Polymeric vanadyl species determine the low-temperature activity of V-based catalysts for the SCR of NO_x with NH_3. *Sci. Adv.* **4**, eaau4637 (2018).
7. Gevers, L. et al. Unraveling the structure and role of Mn and Ce for NO_x reduction in application-relevant catalysts. *Nat. Commun.* **13**, 2960 (2022).
8. Inomata, Y. et al. Bulk tungsten-substituted vanadium oxide for low-temperature NO_x removal in the presence of water. *Nat. Commun.* **12**, 557 (2021).
9. Marberger, A. et al. VO_x surface coverage optimization of V_2O_5/WO_3-TiO_2 SCR catalysts by variation of the V loading and by aging. *Catalysts* **5**, 1704–1720 (2015).
10. Kwak, J. H. et al. Excellent activity and selectivity of Cu-SSZ-13 in the selective catalytic reduction of NO_x with NH_3. *J. Catal.* **275**, 187–190 (2010).
11. Shao, J. et al. Electrochemical synthesis of ammonia from nitric oxide using a copper–tin alloy catalyst. *Nat. Energy* **8**, 1273–1283 (2023).
12. Liang, J. et al. Amorphous boron carbide on titanium dioxide nanobelt arrays for high-efficiency electrocatalytic NO reduction to NH_3. *Angew. Chem. Int. Ed.* **61**, e202202087 (2022).
13. Zhang, L. et al. High-performance electrochemical NO reduction into NH_3 by MoS_2 nanosheet. *Angew. Chem. Int. Ed.* **60**, 25263–25268 (2021).
14. John, J. et al. The why and how of NO_x electroreduction to ammonia. *Nat. Catal.* **6**, 1125–1130 (2023).
15. Salmon, N. et al. Offshore green ammonia synthesis. *Nat. Synth.* **2**, 604–611 (2023).
16. Gao, R. et al. Photoelectrochemical production of disinfectants from seawater. *Nat. Sustain.* **8**, 672–681 (2025).
17. Gao, R. et al. Ru-P pair sites boost charge transport in hematite photoanodes for exceeding 1% efficient solar water splitting. *PNAS* **120**, e2300493120 (2023).
18. Gao, R. et al. Dynamic semiconductor-electrolyte interface for sustainable solar water splitting over 600 hours under neutral conditions. *Sci. Adv.* **9**, eade4589 (2023).
19. Wang, D. et al. Hexagonal cobalt nanosheets for high-performance electrocatalytic NO reduction to NH_3. *J. Am. Chem. Soc.* **145**, 6899–6904 (2023).
20. Wu, Z. et al. Cu@Co with dilatation strain for high-performance electrocatalytic reduction of low-concentration nitric oxide. *Adv. Mater.* **36**, 2309470 (2024).
21. Li, Y. et al. Electrocatalytic reduction of low-concentration nitric oxide into ammonia over Ru nanosheets. *ACS Energy Lett.* **7**, 1187–1194 (2022).
22. Guo, X. et al. Aqueous electroreduction of nitric oxide to ammonia at low concentration via vacancy engineered FeOCl. *Angew. Chem. Int. Ed.* **63**, e202318792 (2024).
23. Guo, X. et al. Enhancing low-concentration electroreduction of NO to NH_3 via potential-controlled active site-intermediate interactions. *Angew. Chem. Int. Ed.* **64**, e202420346 (2025).
24. Wang, D. et al. Ru-incorporation-induced phase transition in Co nanoparticles for low-concentration nitric oxide electroreduction to ammonia at low potential. *Adv. Mater.* **36**, 2408580 (2024).
25. Wang, D. et al. Oxygen-bridged copper-iron atomic pair as dual-metal active sites for boosting electrocatalytic NO reduction. *Adv. Mater.* **35**, 2304646 (2023).
26. Liang, J. et al. Coupling denitrification and ammonia synthesis via selective electrochemical reduction of nitric oxide over Fe_2O_3 nanorods. *J. Mater. Chem. A* **10**, 6454 (2022).
27. Wu, T. et al. Greatly improving electrochemical N_2 reduction over TiO_2 nanoparticles by iron doping. *Angew. Chem. Int. Ed.* **58**, 18449–18453 (2019).
28. Kang, W. et al. Structural evidence for a dynamic metallocofactor during N_2 reduction by Mo-nitrogenase. *Science* **368**, 1381 (2020).
29. Wang, C. et al. Advanced noble-metal/transition-metal/metal-free electrocatalysts for hydrogen evolution reaction in water-electrolysis for hydrogen production. *Coord. Chem. Rev.* **514**, 215899 (2024).
30. Gao, R. et al. Single-atomic-site platinum steers photogenerated charge carrier lifetime of hematite nanoflakes for photoelectrochemical water splitting. *Nat. Commun.* **14**, 2640 (2023).
31. Li, J. et al. Identification of durable and non-durable FeN_x sites in Fe–N–C materials for proton exchange membrane fuel cells. *Nat. Catal.* **4**, 10–19 (2021).
32. Spivey, T. D. et al. Selective Interactions between free-atom-like d-States in single-atom alloy catalysts and near-frontier molecular orbitals. *J. Am. Chem. Soc.* **143**, 11897–11902 (2021).
33. Wan, X. et al. Iron atom–cluster interactions increase activity and improve durability in Fe–N–C fuel cells. *Nat. Commun.* **13**, 2963 (2022).
34. Xian, J. et al. Electrocatalytic synthesis of essential amino acids from nitric oxide using atomically dispersed Fe on N-doped carbon. *Angew. Chem. Int. Ed.* **62**, e202304007 (2023).
35. Nie, N. et al. Superfast synthesis of densely packed and ultrafine Pt-lanthanide@KB via solvent-free microwave as efficient hydrogen evolution electrocatalysts. *Small* **17**, 2102879 (2021).
36. Gao, X. et al. Mechanism of particle-mediated inhibition of demetalation for single-atom catalytic sites in acidic electrochemical environments. *J. Am. Chem. Soc.* **145**, 15528–15537 (2023).
37. Kim, D. et al. Selective electrochemical reduction of nitric oxide to hydroxylamine by atomically dispersed iron catalyst. *Nat. Commun.* **12**, 1856 (2021).
38. Yao, Y. et al. Electrochemical nitrogen reduction reaction on ruthenium. *ACS Energy Lett.* **4**, 1336–1341 (2019).
39. Fang, J. et al. Ampere-level current density ammonia electrochemical synthesis using CuCo nanosheets simulating nitrite reductase bifunctional nature. *Nat. Commun.* **13**, 7899 (2022).
40. Li, J. et al. Efficient ammonia electrosynthesis from nitrate on strained ruthenium nanoclusters. *J. Am. Chem. Soc.* **142**, 7036–7046 (2020).
41. Wang, Y. et al. Phase-regulated active hydrogen behavior on molybdenum disulfide for electrochemical nitrate-to-ammonia conversion. *Angew. Chem. Int. Ed.* **63**, e202315109 (2024).
42. Chen, X. et al. Demystify the unique hydrogen spillover effect in electrocatalytic hydrogen evolution. *Green. Chem.* **27**, 4959 (2025).
43. Feng, Y. et al. Electronic metal-support interaction induces hydrogen spillover and platinum utilization in hydrogen evolution reaction. *Angew. Chem. Int. Ed.* **64**, e202413417 (2025).
44. Zhou, J. et al. Linear adsorption enables NO selective electroreduction to hydroxylamine on single Co sites. *Angew. Chem. Int. Ed.* **62**, e202305184 (2023).
45. Han, S. et al. Ultralow overpotential nitrate reduction to ammonia via a three-step relay mechanism. *Nat. Catal.* **6**, 402–414 (2023).
46. Chen, K. et al. Self-tandem electrocatalytic NO reduction to NH_3 on a W single-atom catalyst. *Nano Lett.* **23**, 1735–1742 (2023).
47. Cheon, S. et al. Electro-synthesis of ammonia from dilute nitric oxide on a gas diffusion electrode. *ACS Energy Lett.* **7**, 958–965 (2022).
48. Li, M. et al. A pair-electrosynthesis for formate at ultra-low voltage via coupling of CO_2 reduction and formaldehyde oxidation. *Nano-Micro Lett.* **14**, 211 (2022).
49. Zhu, D. et al. Photo-illuminated diamond as a solid-state source of solvated electrons in water for nitrogen reduction. *Nat. Mater.* **12**, 836–841 (2013).
50. Mortensen, J. J. et al. Real-space grid implementation of the projector augmented wave method. *Phys. Rev. B* **71**, 035109 (2005).
51. Enkovaara, J. et al. Electronic structure calculations with GPAW: a real-space implementation of the projector augmented-wave method. *J. Phys. Condens. Matter* **22**, 253202 (2010).

52. Held, A. et al. Simplified continuum solvent model with a smooth cavity based on volumetric Data. *J. Chem. Phys.* **141**, 174108 (2014).
53. Peterson, A. A. Global optimization of adsorbate-surface structures while preserving molecular identity. *Top. Catal.* **57**, 40–53 (2014).
54. Larsen, A. H. et al. The atomic simulation environment—a Python library for working with atoms. *J. Phys. Condens. Matter* **29**, 273002 (2017).
55. Norskov, J. K. et al. Origin of the overpotential for oxygen reduction at a fuel-cell cathode. *J. Phys. Chem. B* **108**, 17886–17892 (2004).
56. Woo, T. K. et al. A combined car–Parrinello QM/MM implementation for Ab initio molecular dynamics simulations of extended systems: application to transition metal catalysis. *J. Phys. Chem. B* **101**, 7877–7880 (1997).
57. Jarzynski, C. et al. Nonequilibrium equality for free energy differences. *Phys. Rev. Lett.* **78**, 2690–2693 (1997).

Acknowledgements

This work was supported by National Natural Science Foundation of China (Nos. 52202214, 22072015, 21927811, and 22376222), Natural Science Foundation of Sichuan Province (No. 2023NSFSC0954), China National Postdoctoral Program for Innovative Talents (No. BX2021053), the Science and Technology lnnovation Program of Hunan Province (No. 2023RC1012), Central South University Research Program of Advanced Interdisciplinary Studies (No. 2023QYJC012), and China Postdoctoral Science Foundation (No. 2021M700680). The authors thank BL11B beamline of the Shanghai Synchrotron Radiation Facility (SSRF) for providing the XAFS beamtime. The numerical calculations in this paper have been done on Computing Center in Xi'an.

Author contributions

T.W. and X.G. conceived the idea, wrote the original draft, and collected and analyzed the data. X.G. and T.W. performed the DFT calculations and experiments. C.M. provided the HAADF-STEM characterization. M.L. supervised this project. All authors contributed and reviewed the manuscript.

Competing interests

The authors declare no competing interests.

Additional information

Supplementary information The online version contains supplementary material available at https://doi.org/10.1038/s41467-025-63365-7.

Correspondence and requests for materials should be addressed to Min Liu.

Peer review information *Nature Communications* thanks Xianbiao Fu, Rui-Ting Gao, Xin Wang and the other anonymous reviewer(s) for their contribution to the peer review of this work. A peer review file is available.

[1]Hunan Joint International Research Center for Carbon Dioxide Resource Utilization, State Key Laboratory of Powder Metallurgy, School of Physics, Central South University, Changsha, China. [2]Precision Medicine Translational Research Center, West China Hospital, Sichuan University, Chengdu, China. [3]School of Materials Science and Engineering, Central South University, Changsha, China. [4]Institute of Fundamental and Frontier Sciences, University of Electronic Science and Technology of China, Chengdu, Sichuan, China. [5]College of Materials Science and Engineering, Hunan University, Changsha, China. [6]School of Metallurgy and Environment, Central South University, Changsha, China. [7]Department of Electrical and Electronic Engineering, The Hong Kong Polytechnic University, Hong Kong, China. [8]These authors contributed equally: Xiaoxi Guo, Tongwei Wu. ✉e-mail: minliu@csu.edu.cn